

1                   **The conductive cooling of planetesimals with**  
2                   **temperature-dependent properties**

3                   **M. Murphy Quinlan<sup>1</sup>, A. M. Walker<sup>1</sup>, C. J. Davies<sup>1</sup>, J. E. Mound<sup>1</sup>, T.**  
4                   **Müller<sup>1,2</sup>, J. Harvey<sup>1</sup>**

5                                   <sup>1</sup>School of Earth and Environment, University of Leeds, Leeds, UK  
6                                   <sup>2</sup>Geoscience Center, Georg-August-University Göttingen, Göttingen, Germany

7                   **Key Points:**

- 8                   • Conductivity, heat capacity and density are temperature dependent and control  
9                   the cooling of planetesimals  
10                  • Conductive cooling models of meteorite parent bodies frequently approximate these  
11                  properties as constant  
12                  • Temperature-dependence in a model of the pallasite parent body delays the on-  
13                  set of core solidification by 40 million years

---

Corresponding author: Maeve Murphy Quinlan, [eeemmq@leeds.ac.uk](mailto:eeemmq@leeds.ac.uk)

**Abstract**

Modelling the planetary heat transport of small bodies in the early Solar System allows us to understand the geologic context of meteorite samples. Conductive cooling in planetesimals is controlled by thermal conductivity and volumetric heat capacity, which are functions of temperature ( $T$ ). We investigate if the incorporation of the  $T$ -dependence of thermal properties and the introduction of a non-linear term to the heat equation could result in different interpretations of the origin of different classes of meteorites. We have developed a finite difference code to perform numerical models of a conductively cooling planetesimal with  $T$ -dependent properties and find that including  $T$ -dependence produces considerable differences in thermal history, and in turn the estimated timing and depth of meteorite genesis. We interrogate the effects of varying the input parameters to this model and explore the non-linear  $T$ -dependence of conductivity with simple linear functions before applying non-monotonic functions for conductivity and volumetric heat capacity fitted to published experimental data. For a representative calculation of a 250 km radius pallasite parent body,  $T$ -dependent properties delay the onset of core crystallisation and dynamo activity by  $\sim 40$  Myr, approximately equivalent to increasing the planetary radius by 10%, and extends core crystallisation by  $\sim 3$  Myr. This affects the range of planetesimal radii and core sizes for the pallasite parent body that are compatible with paleomagnetic evidence. This approach can also be used to model the  $T$ -evolution of other differentiated minor planets and primitive meteorite parent bodies and constrain the formation of associated meteorite samples.

**Plain Language Summary**

Meteorites are fragments of the earliest planetary building blocks in our Solar System. These small planetary bodies (planetesimals) were a few tens to hundreds of km across. Different types of meteorites came from different planetesimals of various sizes. Some types of meteorites formed near the surface of their parent bodies, while others are derived from deep within the planetesimal, where it stayed hotter for longer. Understanding how quickly these planetesimals cooled allows us to match the cooling rates recorded within meteorites to different depths inside their parent body: the rock that formed the meteorite would have cooled rapidly near the surface and more slowly nearer the centre.

Properties such as thermal conductivity, heat capacity and density control how quickly planetesimals cool down. These properties are temperature dependent, meaning their value changes as the temperature of the material changes. If we understand these properties, we can better model how quickly planetesimals cooled in the early solar system. Previous models have often approximated these effects with constant values. In this work we use properties that change as the temperature of the planetesimal changes, and investigate how much of an impact this makes on the cooling history.

We find that temperature dependent properties produce different results to constant values, which can lead to different estimations of the size of the parent body for certain meteorites, whether some groups of meteorites formed in the same body, and when the core of these parent bodies may have frozen solid.

**1 Introduction**

Planetesimals are small rocky or icy bodies of a few to a few hundred kilometres in diameter that formed through coagulation of dust grains in the protoplanetary disk, and are considered the building blocks of larger planetary bodies (Kokubo & Ida, 2012). These early planetesimals are hypothesised to be the primary parent bodies of meteorites while the remnants of disrupted planetesimals, preserved as asteroids, are termed the secondary parent bodies (Greenwood et al., 2020). Planetesimals experienced varied ther-

mal histories: differentiated meteorites displaying igneous textures are sourced from planetesimals that underwent melting and segregation of a metallic core and silicate mantle (Baker et al., 2005), while chondritic meteorites contain primitive material including solids that condensed from hot gas in the Solar Nebula (MacPherson, 2014). Understanding the geological context of differentiated meteorites and their parent bodies' thermal evolution allows constraints to be placed on the formation, differentiation and eventual breakup of planetesimals, and on the early evolution of the Solar System. In this context, models of conductive cooling of differentiated primary parent bodies are frequently used to aid the interpretation of meteorite samples. In this study we investigate the importance of including temperature dependent thermal properties in such models. We use a pallasite parent body as an example to illustrate the influence including  $T$ -dependent properties can have on understanding the origin of meteorite samples.

One approach to understanding the formation of meteorites is to analyse the thermal processing experienced by meteorite samples and to compare this to estimated temperature conditions within the parent body using thermal evolution models. Heat flow in conductively cooling planetesimals is controlled by the material properties of their constituent minerals — thermal conductivity ( $k$ ), density ( $\rho$ ) and heat capacity ( $C$ ), in addition to the boundary conditions imposed and the geometry of the planetesimal. Large temperature gradients are expected in planetesimals, with typical surface temperatures of  $\sim 250$  K rising to  $\sim 1800$  K at the centre (Bryson et al., 2015; Scheinberg et al., 2015). Planetesimals are low pressure environments, with a gradient of  $\sim 0.3$  GPa calculated across a 250 km radius silicate body with a 125 km radius iron core (see hydrostatic equilibrium calculation in supplementary information). If  $k$ ,  $\rho$  and  $C$  are assumed constant, they can be expressed in terms of diffusivity  $\kappa = \frac{k}{\rho C}$ . This is a common approximation made in conductive cooling models of differentiated planetesimals despite temperature and pressure dependence (Bryson et al., 2015; Fu et al., 2014; Haack et al., 1990; Tarduno et al., 2012). While the finite difference methods frequently used in these models can be applied to systems involving  $T$ -dependent properties, the heat conduction equation becomes nonlinear and more expensive to solve when  $T$ -dependent  $k$  is included (Öziskik, 1993). Conductivity decreases by 40 – 60 % of its original value in metamorphic and igneous rocks when temperature increases from room temperature to 1273 K, while conductivity increases by approximately 4 % with an increase in pressure of 1 GPa (Hofmeister, 1999; Seipold, 1998; Wen et al., 2015). Due to the weaker dependence of conductivity on pressure, and the low pressure gradients expected in planetesimals, in this paper we will focus on the temperature dependence of material properties.

In solids at low temperatures ( $T < \theta_D$ , the Debye temperature), heat capacity increases from zero at 0 K as  $C_v \sim AT^3$ , where  $C_v$  is specific heat capacity at a constant volume and  $A$  is a constant (Debye, 1912). At high temperatures ( $T > \theta_D$ ), heat capacity is weakly dependent on temperature and can be approximated with a constant value (Petit & Dulong, 1819). This results in approximately 30 % increase in  $C$  over the temperature range commonly modelled for planetesimals (Figure 1).

In electrically insulating solids such as mantle silicates, heat is primarily transferred through lattice or phonon conduction. As temperature increases, the mean energy per phonon also increases due to the change in phonon specific heat. At lower temperatures ( $T < \theta_D$ ), the inelastic phonon relaxation time is constant as scattering is primarily due to crystal defects or boundaries. This results in  $k \propto T^3$  due to the  $T$ -dependence of  $C$  (Hofmeister, 1999; Poirier, 2000). When phonon momentum exceeds a threshold at high temperatures, phonon–phonon Umklapp scattering acts to reduce  $k$ , producing a  $k \propto \frac{1}{T}$  dependency (Poirier, 2000). This non-monotonic behaviour is illustrated in Figure 1.

A change in density with temperature can be linked to thermal expansion by the coefficient of expansivity,  $\alpha$ :  $\rho = \rho_0 - \alpha\rho_0(T - T_0)$ , where  $\rho_0$  is a reference density at  $T_0$ , commonly room temperature ( $\sim 295$  K). Density is less temperature dependent than

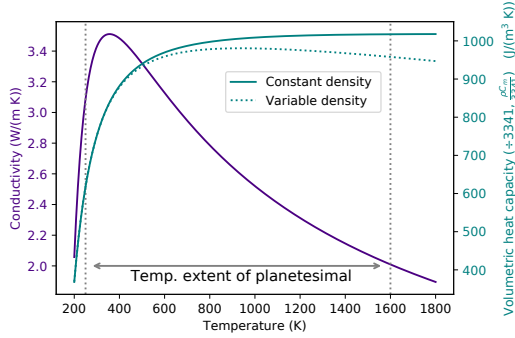


**Figure 1.** Temperature dependent material properties of olivine. As the temperature dependence of density ( $\rho$ ) is small, heat capacity ( $C$ ) and density are combined as volumetric heat capacity and are shown with a constant and  $T$ -dependent  $\rho$  to highlight the effect; both are divided by the value of the constant density,  $\rho_0 = 3341 \text{ kg m}^{-3}$ . These experimental functions are discussed further in section 2. Data from: Fei (2013); Robie et al. (1982); Su et al. (2018); Suzuki (1975); Xu et al. (2004).

116  $C$  or  $k$ , and is combined with heat capacity in Figure 1 as volumetric heat capacity, both  
 117 as a constant and as a  $T$ -dependent function to illustrate the scale of its effect.

118 Previous models of planetesimal thermal evolution take various approaches to the  
 119 incorporation of  $k$ ,  $\rho$  and  $C$ . These models address different stages of planetesimal evolu-  
 120 tion, depending on the meteorite group of interest, and can be broadly grouped into  
 121 two classes. Models focusing on the accretion, early heating and melting of asteroids and  
 122 planetoids investigate the origin of primitive meteorites (Allan & Jacobs, 1956; Elkins-  
 123 Tanton et al., 2011; Hevey & Sanders, 2006), while conductive cooling models examine  
 124 the post-peak- $T$  period following recrystallisation and capture the genesis of extensively  
 125 differentiated meteorites such as pallasites (Bryson et al., 2015; Ghosh & McSween, 1999;  
 126 Haack et al., 1990; Tarduno et al., 2012). Models in the first class, for example those in-  
 127 vestigating the ordinary chondrite parent body, often employ temperature-dependent dif-  
 128 fusivity from Yomogida and Matsui (1983):  $\kappa = A + B/T$ , where  $A$  and  $B$  are terms  
 129 that describe the degree of compaction of the parent body (Akridge et al., 1998; Ben-  
 130 nnett & McSween, 1996; Harrison & Grimm, 2010). Ghosh and McSween (1999) highlight  
 131 the importance of incorporating a temperature-dependent specific heat capacity in the  
 132 modelling of primitive asteroids, recording a decrease in peak temperatures and corre-  
 133 sponding change in closure temperatures when  $T$ -dependent  $C$  is used, but hold  $k$  and  
 134  $\rho$  constant.

135 The second class of models, which address conductive cooling in differentiated plan-  
 136 etesimals such as the primary pallasite parent body (Bryson et al., 2015), generally as-  
 137 sume  $k$ ,  $\rho$  and  $C$  are independent of temperature. When experimentally investigating  
 138 the effect of Fe content on olivine conductivity, Zhang et al. (2019) comment on the in-  
 139 clusion of  $T$ -dependent and composition-dependent  $k$  in their COMSOL<sup>TM</sup> models and  
 140 note that the inclusion of variable properties have a non-negligible effect on the thermal  
 141 evolution of a silicate sphere. However, the focus of the study is olivine forsterite con-  
 142 tent and the impact of olivine composition on the thermal evolution of planetary bod-  
 143 ies, and  $T$ -dependence is not systematically explored. The implications of neglecting  $T$ -  
 144 dependent  $k$ ,  $\rho$  and  $C$  on the interpretation of meteorite parent body models is not un-  
 145 derstood.

146 The pallasite parent body has been chosen as an example for this study as previ-  
 147 ous research has tied paleomagnetism identified in meteorite samples to the period of  
 148 core crystallisation in the parent body (Bryson et al., 2015; Tarduno et al., 2012). In or-  
 149 der for the metal portion of a pallasite meteorite to record a convectational core dynamo,  
 150 it must cool through the Curie temperature of its metal portion while the core is crys-  
 151 tallising. Modifying the material properties of the body affects whether this condition  
 152 is met. This places an easily-testable constraint on models to investigate the importance  
 153 of including  $T$ -dependent properties when deciding parent body geometry, the forma-  
 154 tion depth of pallasite meteorites, and the number of parent bodies required.

155 Before we address the specific example of the pallasite parent body, we outline the  
 156 approach used to incorporate  $T$ -dependent properties in models of conductive cooling  
 157 of planetesimals and show how, even in simple cases, this can have an important influ-  
 158 ence on their thermal history. We first address the model and numerical scheme in sec-  
 159 tion 2, before exploring the sensitivity of the model to different parameters with  $k$ ,  $C$   
 160 and  $\rho$  as independent of  $T$  and investigating the range of parameters used in the liter-  
 161 ature. We then address the incorporation of a non-linear term when  $T$ -dependent  $k$  is  
 162 included by using a series of simple linear functions for  $k(T)$  in section 3.2. We imple-  
 163 ment  $T$ -dependent functions for  $k$ ,  $C$  and  $\rho$  in section 3.3, and attempt to recreate these  
 164 results by averaging the values for  $k$ ,  $C$  and  $\rho$  radially and through time and then us-  
 165 ing these mean values in the constant model. Finally, we discuss the relevance to mod-  
 166 elling the pallasite parent body.

## 167 2 Methods

168 To investigate the effect of including temperature-dependent properties in the ther-  
 169 mal evolution of planetesimals, we used the 1D in radius  $r$  heat conduction equation with  
 170 a non-linear term to allow for temperature dependence of  $k$ ,  $\rho$  and  $C$  (Carslaw & Jaeger,  
 171 1986; Özisik, 1993). As in Bryson et al. (2015), the layered body is composed of three  
 172 primary materials: a metallic FeS core which is initially molten, a solid olivine mantle  
 173 and an insulating regolith layer (see Figure 2). Assuming a purely conductive mantle fol-  
 174 lowing magma-ocean solidification, in which convective heat transport is neglected, the  
 175 temperature  $T$  in the mantle satisfies the differential heat conduction equation in spher-  
 176 ical geometry:

$$\frac{\partial T}{\partial t} \rho C = \frac{1}{r^2} \frac{\partial}{\partial r} \left( kr^2 \frac{\partial T}{\partial r} \right) = \overbrace{\frac{dk}{dT} \left( \frac{\partial T}{\partial r} \right)^2}^{\text{non-linear term}} + \underbrace{\frac{2k}{r} \frac{\partial T}{\partial r}}_{\text{geometric term}} + \overbrace{k \frac{\partial^2 T}{\partial r^2}}^{\text{linear term}}, \quad (1)$$

177 where  $t$  is time. The non-linear term arises due to the  $T$ -dependence of  $k$ . The insulat-  
 178 ing regolith layer is given a constant diffusivity lower than that of the mantle as in Bryson  
 179 et al. (2015). Pressure and self-gravitation are not incorporated into the current model.  
 180 The boundary and initial conditions are chosen as follows:

$$T(r_p, t) = T_{\text{surf}}, \quad T(r, t_0) = T_{\text{init}}, \quad T(r_c, t) = T_c(t), \quad (2)$$

181 where  $r_p$  is the planetesimal radius,  $r_c$  is the core radius,  $T_{\text{surf}}$  is the constant surface  
 182 temperature,  $T_c$  is the core temperature and  $T_{\text{init}}$  is the initial temperature, implying  
 183 an homogeneous initial interior temperature distribution at  $t_0$ ; the code can accommo-  
 184 date a heterogeneous initial temperature array but this is not used in this study. A Dirich-  
 185 let boundary condition has been applied to the surface as in Bryson et al. (2015) instead  
 186 of a radiative condition as used by Ghosh and McSween (1998), assuming the temper-  
 187 ature at the surface of the planetesimal is constant and that of the ambient Solar nebu-  
 188 la. While a radiative boundary condition is a closer approximation to the physical sys-

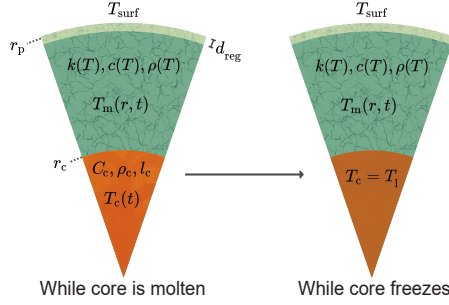


**Figure 2.** Not to scale. General model set-up, both before and during core solidification, displaying the functions relevant to different regions. Core radius is defined as a fraction of the total planetary radius, which includes the regolith layer. The regolith has a constant  $\kappa$ .

189 tem, a simpler fixed-temperature boundary condition has been found to produce neg-  
190 ligible difference in inner-Solar System asteroidal models (Hevey & Sanders, 2006; Moskovitz  
191 & Gaidos, 2011).

The boundary condition for the base of the mantle depends on the core temperature. The core is assumed to be entirely liquid and vigorously convecting when molten (Bryson et al., 2015; Tarduno et al., 2012). The core temperature is updated by considering the total energy extracted across the core-mantle boundary (CMB). The energy transferred during a small time increment  $\delta t$  is

$$E_{CMB} = -A_c k_{CMB} \left. \frac{\partial T}{\partial r} \right|_{r=r_c} \delta t, \quad (3)$$

192 where  $A_c$  is the surface area of the core,  $r_c$  is the radius of the core, and  $k_{cmb}$  is the thermal  
193 conductivity at the base of the mantle at the CMB, i.e.  $k_{CMB} = k_m(T(r_c, t))$ . As  
194  $E_{CMB} = \rho_c V_c C_c \Delta T$  where  $V_c$  is the total volume of the core and  $\Delta T$  is change in tem-  
195 perature, the change in the core temperature in one time increment ( $\Delta T_C$ ) is:

$$\Delta T_C = \frac{A_c k_{CMB} \left. \frac{\partial T}{\partial r} \right|_{r=r_c} \delta t}{\rho_c C_c V_c} = \frac{3 k_{CMB} \left. \frac{\partial T}{\partial r} \right|_{r=r_c} \delta t}{\rho_c C_c r_c}. \quad (4)$$

196 The temperature at the base of the mantle is then updated by adding  $\Delta T$  to the tem-  
197 perature at the previous timestep:

$$T_{CMB}(r_c, t) = T_{CMB}(r_c, t - \delta t) + \Delta T_c. \quad (5)$$

198 The core cools as the mantle conducts heat to the surface, and is assumed to solidify when  
199  $T_c$  reaches the melting temperature of the FeS core ( $T_l$ , in this case  $T_l = 1200$  K, Bryson  
200 et al. (2015)). Once the core begins to freeze, the temperature is constant at  $T_l$  as latent  
201 heat is extracted across the CMB. The liquid and solid fraction act identically during  
202 this process and partitioning of elements is not addressed during freezing. The core  
203 solidifies entirely once the total latent heat associated with crystallisation has been ex-  
204 tracted — when  $E_{CMB}$  during the solidification period exceeds  $E_l$ , where the total latent  
205 heat of the core is:

$$E_l = m_c L_c = \frac{4}{3} \pi r_c^3 \rho_c L_c, \quad (6)$$

206 where  $m_c$  is the mass of the core and  $L_c$  the specific latent heat of fusion of the core (Bryson  
207 et al., 2015; Tarduno et al., 2012).

208

## 2.1 Numerical Implementation

209

210

211

We solve the conduction equation numerically for the mantle using an explicit finite difference scheme with first order differences in time and second order in space. Equation 1 can be rewritten with the temperature at radius  $r$  and time  $t$  denoted by  $T_r^t$ :

$$T_r^t = T_r^{t-\delta t} + \frac{1}{\rho C} \delta t \times \left( \underbrace{\left. \frac{dk}{dT} \right|_r^{t-\delta t} \frac{(T_{r+\delta r}^{t-\delta t} - T_{r-\delta r}^{t-\delta t})^2}{4\delta r^2}}_{\text{non-linear term}} + \overbrace{\frac{k}{r\delta r} (T_{r+\delta r}^{t-\delta t} - T_{r-\delta r}^{t-\delta t})}^{\text{geometric term}} + \underbrace{\frac{k}{\delta r^2} (T_{r+\delta r}^{t-\delta t} - 2T_r^{t-\delta t} + T_{r-\delta r}^{t-\delta t})}_{\text{linear term}} \right), \quad (7)$$

where  $\delta t$  and  $\delta r$  are the constant timestep and radius step, and  $k$  is evaluated at  $T_r^{t-\delta t}$ . A consequence of this discretisation is that temperature dependent properties lag if evaluated at  $t - \delta t$ . A more accurate method is to evaluate  $k$  as

$$k^t = k^{t-\delta t} + \left( \frac{\partial k}{\partial T} \right)^{t-\delta t} (T^{t-\delta t} - T^{t-2\delta t}), \quad (8)$$

212

213

214

215

216

217

218

219

220

and similarly for  $C$  and  $\rho$  (Özışık, 1993). To reduce the error associated with variable  $k$  not being centred in time, we chose a sufficiently small  $\delta t$  such that  $k(T_r^{t-\delta t}) \approx k(T_r^t)$ , within a defined error ( $< 1\%$  of  $k$ ). We compared this with a selection of runs using the more accurate but computationally expensive method above for  $k^t$  and  $C\rho^t$ , and the differences in results were negligible. The maximum timestep allowable for stability in this numerical method must satisfy Von Neumann stability criteria, discussed in the supplementary information. This numerical solution, with constant  $k$ ,  $C$  and  $\rho$ , was compared with an analytical solution from Crank (1979) which is also described in the supplementary information.

221

## 2.2 Meteorite formation depth

222

223

224

225

226

227

228

229

230

To illustrate the implications of this study on the pallasite parent body, we calculate the formation depths of pallasite meteorite samples, Imilac and Esquel, using the method and recorded cooling rates of Bryson et al. (2015). The FeNi portion of pallasite meteorites records the cooling rate of the sample at 800 K (J. Yang et al., 2010). The intersection between the cooling rate contour and the 800 K isotherm gives a formation depth. Then, the time when this depth passes through the tetrataenite formation temperature (593 K) and is magnetically recording can be compared to the timing of core crystallisation to see if it occurs while the core is freezing, thus potentially recording core dynamo activity (Bryson et al., 2015).

231

## 2.3 Parameter choices for the pallasite parent body

232

233

234

235

236

237

238

239

240

241

We selected parameters from previous models of planets, planetesimals and asteroids in the literature and experimental results from geochemistry and mineral physics studies as detailed in Table 1. For many of these parameters, we have chosen both a reference value relevant to our example case of the pallasite parent body, and a range of values used in other models of differentiated planetesimals with different assumptions regarding geometry and composition. Reference values related to the geometry of the planetesimal, the core, the boundary conditions and the calculation of meteorite formation depth recreate the model of Bryson et al. (2015), while mantle olivine properties have been chosen from experimental results (Table 1) as Bryson et al. (2015) use a constant  $\kappa$ . While Bryson et al. (2015) use a planetesimal radius  $r_p = 200$  km, we have chosen

**Table 1.** *Model Parameters.*

Symbol	Parameter	Value(s)	Units
$r_p$	Planetesimal radius	<b>250</b> , 150 – 600 <sup>b,d,s</sup>	km
$r_c$	Core radius	<b>50</b> <sup>b,s</sup> , 20 – 80 <sup>q</sup>	% of $r_p$
$d_{\text{reg}}$	Regolith thickness	<b>8</b> <sup>b</sup> , 0 – 20 <sup>i,t</sup>	km
$k$	Mantle conductivity	<b>3</b> <sup>b</sup> , 1.5 – 4 <sup>e,w,aa</sup>	W m <sup>-1</sup> K <sup>-1</sup>
$C$	Mantle heat capacity	<b>819</b> <sup>r</sup> , 600 – 2000 <sup>h,k,n,o,s</sup>	J kg <sup>-1</sup> K <sup>-1</sup>
$\rho$	Mantle density	<b>3341</b> <sup>r</sup> , 2500 – 3560 <sup>l,m,y</sup>	kg m <sup>-3</sup>
$C_c$	Core heat capacity	<b>850</b> <sup>p,z</sup> , 780 – 850 <sup>c,u</sup>	J kg <sup>-1</sup> K <sup>-1</sup>
$\rho_c$	Core density	<b>7800</b> <sup>o</sup> , 7011 – 7800 <sup>c,l,p,u</sup>	kg m <sup>-3</sup>
$\kappa_{\text{reg}}$	Regolith diffusivity	<b>5 × 10<sup>-7</sup></b> <sup>b</sup>	m <sup>2</sup> s <sup>-1</sup>
$L_c$	Latent heat of fusion of core	<b>2.7 × 10<sup>5</sup></b> <sup>g,o</sup> , 2.56 × 10 <sup>5</sup> <sup>p</sup>	J kg <sup>-1</sup>
$T_1$	Freezing temperature of core	<b>1200</b> <sup>b</sup> , 1213 <sup>g,o,s</sup>	K
$T_{\text{init}}$	Initial temperature	<b>1600</b> <sup>b</sup> , 1450 – 1820 <sup>o,p</sup>	K
$T_{\text{surf}}$	Surface temperature	<b>250</b> <sup>j,v</sup> , 150 – 300 <sup>a,f,o</sup>	K
$T_{\text{cz}}$	Tetrataenite formation temp.	593 <sup>b</sup>	K
$T_{\text{cr}}$	Cooling-rate temperature	800 <sup>b,x</sup>	K
$\delta t$	Timestep	1 × 10 <sup>11</sup>	s
$\delta r$	Radial step	1000	m

*Note:* Reference values in **bold**. <sup>a</sup> Boss (1998), <sup>b</sup> Bryson et al. (2015), <sup>c</sup> Davies and Pommier (2018), <sup>d</sup> The OSIRIS-REx Team et al. (2019), <sup>e</sup> Elkins-Tanton et al. (2011), <sup>f</sup> Gail et al. (2014), <sup>g</sup> Ghosh and McSween (1998), <sup>h</sup> Ghosh and McSween (1999), <sup>i</sup> Haack et al. (1990), <sup>j</sup> Hevey and Sanders (2006), <sup>k</sup> Hort (1997), <sup>l</sup> Johnson et al. (2019), <sup>m</sup> Miyamoto et al. (1982), <sup>n</sup> Robie et al. (1982), <sup>o</sup> Sahijpal et al. (2007), <sup>p</sup> Scheinberg et al. (2015), <sup>q</sup> Solomon (1979), <sup>r</sup> Su et al. (2018), <sup>s</sup> Tarduno et al. (2012), <sup>t</sup> Warren (2011), <sup>u</sup> Williams and Nimmo (2004), <sup>v</sup> Woolum and Cassen (1999), <sup>w</sup> Xu et al. (2004), <sup>x</sup> C. W. Yang et al. (1997), <sup>y</sup> Yomogida and Matsui (1983), <sup>z</sup> Young (1991), <sup>aa</sup> Zhang et al. (2019).

242  $r_p = 250$  km as our reference value so that paleomagnetic recording occurs while the  
243 core is crystallising for both samples (section 2.2).

244 Initially, we allowed models to run for 400 million years. We increased the run time  
245 if it did not capture the period of core solidification, for example in cases with larger radii.  
246 The core reverts to an isothermal state following the solidification period. This simpli-  
247 fied approximation of a highly-conductive metallic core is sufficient for the example ap-  
248 plication in this study, for which the post core-solidification period is not of interest.

#### 249 **2.4 Incorporation of temperature dependent properties**

250 For this study, we have chosen the function used for heat capacity in olivine at amb-  
251 bient pressures from Su et al. (2018), based on lattice vibration theory from Berman and  
252 Brown (1985) and fit to experimental data from Isaak (1992):

$$C = 995.1 + \frac{1343}{\sqrt{T}} + \frac{2.887 \times 10^7}{T^2} - \frac{6.166}{T^3}. \quad (9)$$

253 Note that this is valid for the range of temperatures  $T_{\text{surf}} - T_{\text{init}}$ . We don't explore tem-  
254 peratures close to 0 K. The expression for thermal expansivity is also taken from Su et

255 al. (2018) based on the functional fit by Fei (2013) and using experimental data from Suzuki  
256 (1975):

$$\alpha = 3.304 \times 10^{-5} + 0.742 \times 10^{-8}T - 0.538T^{-2}. \quad (10)$$

257 As described in section 1,  $\alpha$  can be used to calculate the change in density with temper-  
258 ature:  $\rho = \rho_0 - \alpha\rho_0(T - T_0)$ , where  $T_0 = 295$  K and  $\rho_0 = 3341$  kg m<sup>-3</sup>.

259 As the lower temperatures modelled ( $\sim 250$  K) are rarely of interest in terrestrial  
260 mineral physics and are less accessible to experimental studies, we constructed a sim-  
261 ple conductivity function for olivine spanning 250 – 1800 K. As discussed in section 1,  
262 conductivity is controlled by different process at high and low temperatures, resulting  
263 in different temperature dependencies. For the high- $T$  region, we used the experimentally-  
264 derived curve from Xu et al. (2004):

$$k = 4.13 \times \left(\frac{298}{T}\right)^{\frac{1}{2}} \times (1 + aP), \quad (11)$$

265 where  $a = 0.032$  GPa<sup>-1</sup> (experimentally derived) and  $P = 4$  GPa. As  $T$ -dependence  
266 of  $k$  at temperatures  $\ll \theta_D$  is similar to that of  $C$ , a function identical in shape to equa-  
267 tion 9 but normalised such that  $C = 1$  at  $T > \theta_D$  was used for the low- $T$  region. As  
268 this low- $T$  curve is constant and equal to 1 above  $\theta_D$ , it can be multiplied by equation  
269 11 to fill in the low- $T$  region without altering the higher- $T$  experimental results. Our re-  
270 sultant function is differentiable and non-monotonic:

$$k = 80.421 \times \left(1.319 \times T^{-\frac{1}{2}} + 0.978 - \frac{28361.765}{T^2} - \frac{6.057 \times 10^{-5}}{T^3}\right) \times T^{-\frac{1}{2}}, \quad (12)$$

271 While the pressures inside the planetesimal are  $\ll 4$  GPa, changing pressure to  $< 1$  GPa  
272 in equation (11) increases conductivity in our composite function by  $< 0.3$  W/(m K)  
273 at all temperatures. As this is outside of the calibration range of the experiments by Xu  
274 et al. (2004) we have chosen not to include this adjustment as it may not be physically  
275 realistic and pressure effects are not the focus of this study, and instead use  $a$  and  $P$  as  
276 quoted by Xu et al. (2004). These functions are illustrated in Figure 1.

277 In order to fully understand the effect of including temperature dependence in our  
278 model, we also constructed a simple linear function for conductivity before investigat-  
279 ing the more complex equation (12):

$$k = k_0 + \beta T, \quad (13)$$

280 where  $k_0$  is a reference conductivity at 0 K and  $\beta$  controls the temperature dependence,  
281 and can be set as positive or negative.  $\beta$  and  $k_0$  must be chosen such that  $k$  does not  
282 become negative over the temperatures explored in the body. In order to contrast a  $T$ -  
283 dependent conductivity with simply setting the average conductivity higher or lower, func-  
284 tions with both positive and negative  $\beta$  were chosen to approximate the same mean con-  
285 ductivity over radius and time. Additionally, the cases were run with and without the  
286 non-linear term. Both  $\rho$  and  $C$  were held constant to isolate the effect of the conduc-  
287 tivity. The regolith layer maintains a constant  $\kappa$  for all model runs including those with  
288 fully variable  $k$ ,  $\rho$  and  $C$ , as after initial rapid equilibration with the surface tempera-  
289 ture, this layer has a constant temperature. The core properties have also been kept con-  
290 stant.

### 3 Results

The model produces arrays of temperature and cooling rate through time and radius. For any radius  $r$ , the linear, geometric and non-linear (if applicable) terms of the heat conduction equation can be plotted against time. Model outputs that are important to the interpretation of meteorites include the initiation and duration of core crystallisation, the depth within the parent body from which the meteorite was derived and when this occurred, and the peak cooling rates reached. In the specific case of the palasite parent body, the calculated depth of formation can then be tracked to see if this region of the parent body passes through the temperature where magnetism is recorded while the core is solidifying, thus potentially recording core dynamo activity.

#### 3.1 Constant $k$ , $\rho$ and $C$

The model was run with constant  $k$ ,  $\rho$  and  $C$  for both the reference parameters in table 1 and the end-member values quoted, if applicable. In addition, parameters were varied by  $\pm 10\%$  of the reference value to gauge the sensitivity of the model to different inputs. The full results of these parameter explorations are tabulated in the supplementary information.

Figure 3 shows the chosen reference case for the constant  $k$ ,  $\rho$  and  $c$ . The linear term initially dominates the cooling, especially in the shallower regions of the body where there is lower curvature (Figure 3a); the geometric term that accounts for the body's spherical geometry is of more relative importance deeper within the body at smaller radii (Figure 3b). Peak cooling rates are higher and are reached marginally earlier in the shallow portion of the body, as the near-surface rapidly equilibrates with the boundary held at 250 K while the temperature anomaly propagates through the mantle to deeper regions with a time delay determined by the diffusion timescale.

The slope of  $T(r)$  from the base of the mantle to the surface is negative for the duration of the model run. Initially,  $T(r)$  is convex upwards but flattens over time and becomes convex downwards as the linear term changes sign: initially within the body  $\frac{\partial^2 T}{\partial r^2}$  is negative for all radii and increases with time, becoming positive at the boundaries first, with this change in sign propagating towards the middle of the mantle. When the core is removed to approximate a solid sphere, this effect is only seen to propagate downwards from the surface boundary as the breaking effect of the core on the cooling of the mantle is not present. The geometric term then drives further cooling after this point (Figure 3).

When the core reaches 1200 K and begins to freeze, the temperature at the CMB is held constant. The fixed core temperature reduces the cooling rate in the mantle sharply; in the deeper regions of the mantle  $-\frac{\partial T}{\partial t}$  drops towards zero as the mantle reaches the same temperature as the core. The effect is less pronounced in the shallow regions as the cooling rate has already slowed significantly and is approaching zero.

The body cools rapidly at the surface, with shallow depths quickly equilibrating with the constant surface temperature (Figure 4). High temperatures are maintained for longer deeper within the body due to the overlying insulating mantle. Using the cooling rates calculated by Bryson et al. (2015), we calculated source depths of 64 km for Esquel and 57 km for Imilac, approximately midway through the mantle (Figure 4 and Table 2).

The geometry of the body is a strong controlling factor on the cooling rate and timing of core crystallisation (Table 2). The planetary radius has the largest effect: increasing the total radius by 10% slows the cooling of the planetesimal at depth and delays the onset of core crystallisation by 38 Myr. When the core fraction is increased, the core begins to freeze 5 Myr earlier as there is less insulating mantle, but takes 4 Myr longer

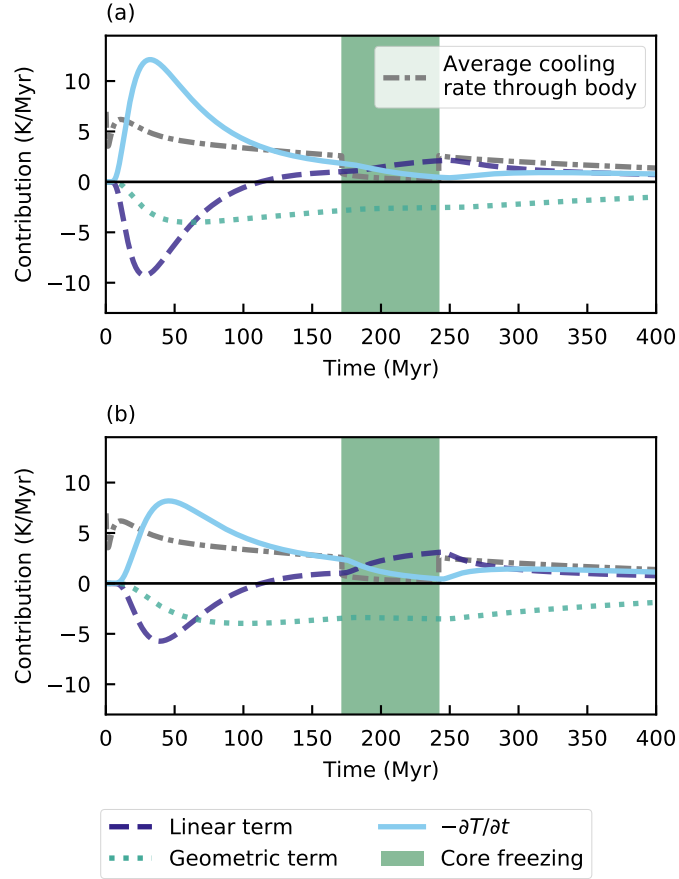


**Figure 3.** Results for the reference case with constant  $k$ ,  $\rho$  and  $C$ . The components of the heat conduction equation are shown at a depth of (a) 42 km (one third of the thickness of the mantle) and (b) 84 km (two thirds). The cooling rate is multiplied by  $-1$  to illustrate how it balances the other components to add to zero. The shaded green area defines the period of core crystallisation.

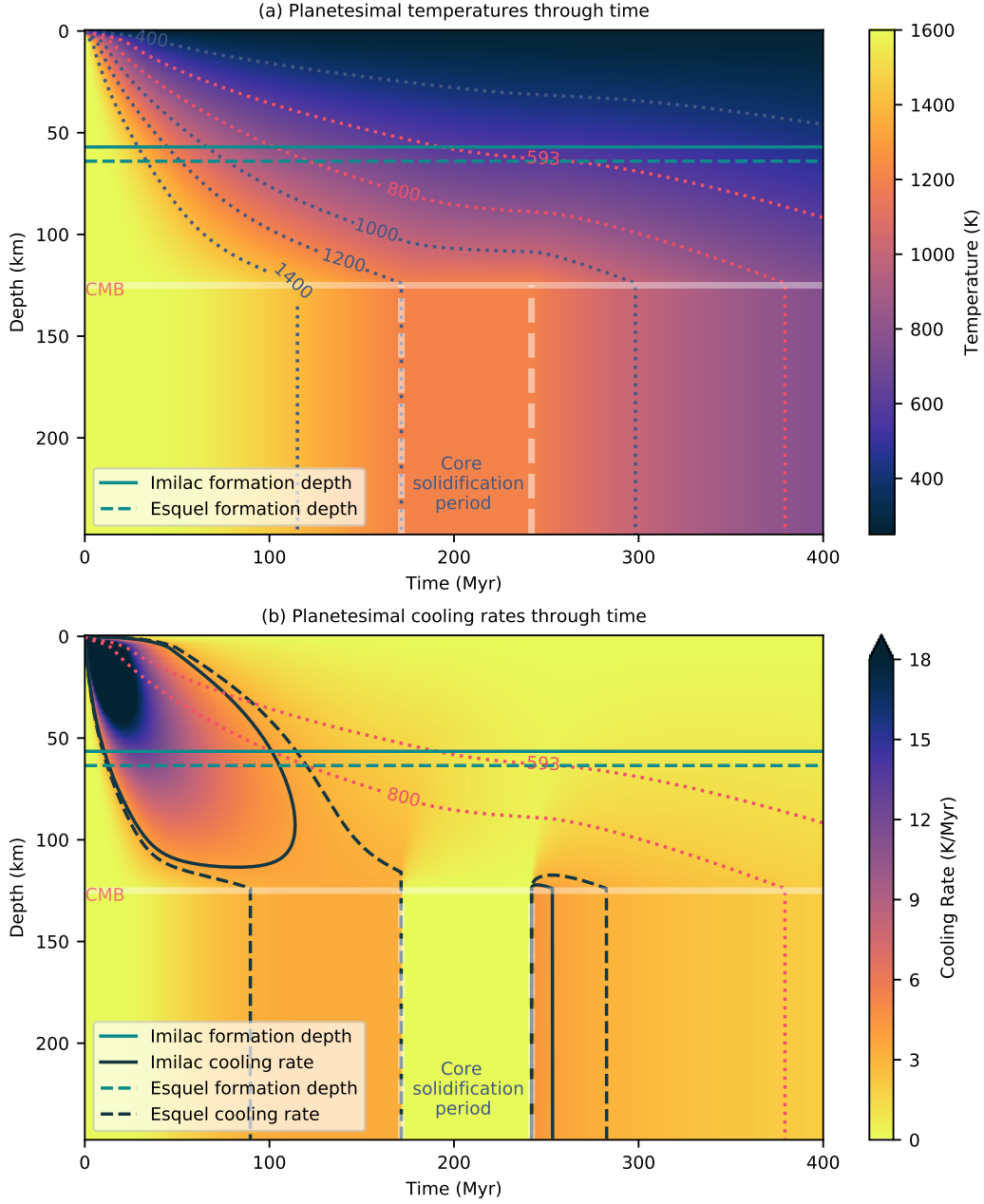


**Figure 4.** Planetesimal (a) temperatures and (b) cooling rates through time for the default model with constant  $k$ ,  $\rho$  and  $c$ . The calculated source depth of the Imilac and Esquel meteorites for this model set-up are shown in both plots, using the cooling rate data and method of Bryson et al. (2015). Temperature contours highlight the tetrataenite formation temperature when paleomagnetism can be recorded (593 K) and the temperature for which the sample’s cooling rates were measured (800 K), while cooling rate contours show the measured cooling rates for both samples.

**Table 2.** *Model results for constant  $k$ ,  $\rho$  and  $C$* 

Varied parameter	Value	Core starts Myr	Core ends Myr	Duration Myr	Esquel depth km	Imilac depth km
Reference case		172	242	70	64	57
$r_p + 10\%$	275 km	210	296	86	64	56
$r_c + 10\%$	138 km	167	241	74	58	53
$r_{\text{reg}} + 1 \text{ km}^a$	9 km	172	242	71	64	57
$k + 10\%$	$3.3 \text{ W m}^{-1} \text{ K}^{-1}$	157	221	64	68	60
$C + 10\%^b$	$901 \text{ J kg}^{-1} \text{ K}^{-1}$	180	252	72	61	54
$k_{\text{max}}$	$4 \text{ W m}^{-1} \text{ K}^{-1}$	132	185	53	77	67
$k_{\text{min}}$	$1.5 \text{ W m}^{-1} \text{ K}^{-1}$	330	400	70	42	36

*Note:* Model results with parameters varied to  $\pm 10\%$  of the default value, with end-member cases included for  $k$ . References for parameter choices given in Table 1. <sup>a</sup>Regolith thickness was increased and decreased by 1 km as 10 % (0.8 km) is smaller than  $\delta r$ . <sup>b</sup>Increasing or decreasing  $C$  or  $\rho$  (not both) by 10 % results in a change in  $\rho C$  by 10 %. Full results in supplementary information.

340 to freeze fully due to its increased size. While the average cooling rate of the body drops  
341 sharply for all cases on initiation of core solidification, the effect is more pronounced when  
342 the core fraction is increased as the cooling rate of the core dominates the overall cool-  
343 ing rate. Increasing the insulating regolith thickness by 1 km while maintaining a 250  
344 km total radius does not delay the onset of core crystallisation, but does increase the du-  
345 ration of the solidification period by 1 Myr. Increasing the regolith thickness further does  
346 delay core solidification, with a 20 km thick regolith causing a 73 Myr delay when com-  
347 pared to the reference case (see supplementary information). The resulting changes in  
348 the calculated source region depth for pallasite meteorites is also shown in Table 2.

349 Increasing  $k$  by 10 % accelerates the cooling in the body, causing the core to be-  
350 gin solidifying 15 Myr earlier. Increasing  $\rho$  or  $C$  by 10 % has the opposite effect, and de-  
351 lays the onset of core crystallisation by 8 Myr. Table 2 also shows the results of setting  
352  $k = 4 \text{ W m}^{-1} \text{ K}^{-1}$  and  $1 \text{ W m}^{-1} \text{ K}^{-1}$ , which reflect the end-member expected values  
353 if  $k$  varied with  $T$  (see Figure 1). Between these two cases, there is a 198 Myr difference  
354 in the timing of the start of core solidification. The core begins to freeze at 132 Myr and  
355 the freezing period lasts 53 Myr when  $k = 4 \text{ W m}^{-1} \text{ K}^{-1}$ , while the core begins to freeze  
356 at 330 Myr when  $k = 1 \text{ W m}^{-1} \text{ K}^{-1}$ . An increase in conductivity results in deeper source  
357 regions for the pallasite meteorites, with the Esquel and Imilac source regions moving  
358 13 and 10 km deeper respectively when  $k = 4 \text{ W m}^{-1} \text{ K}^{-1}$ , while both move  $\sim 22$  km  
359 shallower when  $k = 1 \text{ W m}^{-1} \text{ K}^{-1}$ .

### 360 3.2 Simple linear $T$ -dependent conductivity

361 In this section we explore  $k(T)$  in the form  $k = k_0 + (\beta T)$  with  $\rho$  and  $C$  held con-  
362 stant. For the examples shown in Figure 5 and summarised in table 3, we chose  $\beta = \pm 0.0025$   
363  $\text{W}/(\text{m K}^2)$  and  $k_0$  such that  $k = 3.0 \text{ W}/(\text{m K})$  at the mean temperature of the refer-  
364 ence case with constant  $k$ ,  $\rho$  and  $c$  (with regolith thickness set to 0 km - Table 3) to iso-  
365 late the effect of  $T$ -dependence. The model was run both with and without the non-linear  
366 term in Figures 5a and 5b). When compared to the constant case with  $k = 3 \text{ W}/(\text{m K})$ ,  
367 allowing  $k$  to vary with  $T$  changes the timing and duration of the core crystallisa-

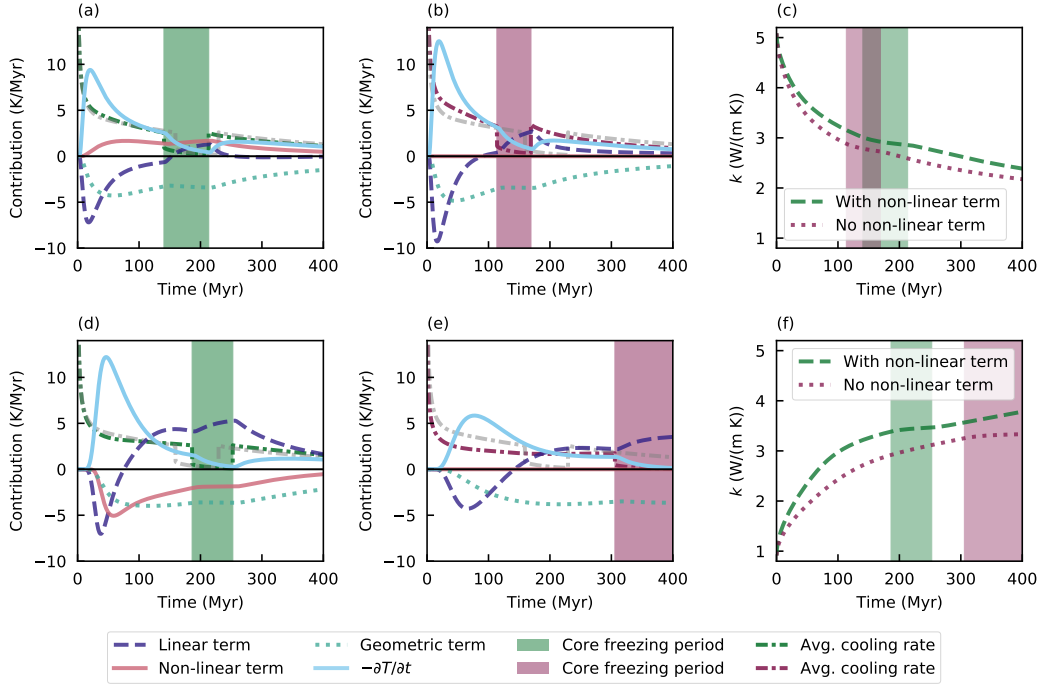


**Figure 5.** Results for model with a linear function for  $k(T)$  and constant  $\rho C$ . Panels (a), (b) and (c) show results for  $\beta = 0.0025$ . Panels (a) and (b) show the components of the heat equation with and without the non-linear term, with the cooling rate averaged across all radii included and compared to the reference case with 9 km regolith. Panel (c) shows the average conductivity through time for both these cases with the core crystallisation period highlighted. Panels (d), (e) and (f) show the equivalent results for  $\beta = -0.0025$ .

368 tion period (see table 3). For  $\beta = 0.0025$  W/(m K<sup>2</sup>) and  $k_0 = 1.1125$  W/(m K) (panel  
 369 (a), Figure 5), the onset of core crystallisation is 19 Myr earlier than for the constant  
 370 case (table 3); in the early stages of the model run the average cooling rate throughout  
 371 the body is higher than the constant case due to higher initial conductivity in the man-  
 372 tle (panel (c) of Figure 5). After  $\sim 80$  Myr (before the core begins to freeze), the aver-  
 373 age cooling rate throughout the body drops below the constant case, resulting in a 3 Myr  
 374 longer core-crystallisation period. The duration of core crystallisation is close to that of  
 375 the constant case as, during this time period, the variable conductivity is similar to the  
 376 fixed conductivity of the constant case (panel (c), Figure 3).

377 When the non-linear term is neglected (panel (b), Figure 5), core crystallisation  
 378 initiates 46 Myr earlier than in the constant reference case, due to increased cooling rates  
 379 despite a lower average conductivity. The non-linear term is always positive and slows  
 380 cooling if  $\beta > 0$ , reducing the peak cooling rates experienced at this depth and the aver-  
 381 age cooling rates in the mantle.

382 The equivalent results for  $\beta = -0.0025$  are shown in panels (d), (e) and (f) of Fig-  
 383 ure 5 and in Table 3. For  $\beta = -0.0025$  W/(m K<sup>2</sup>) and  $k_0 = 4.8875$ , the onset of core  
 384 solidification is delayed by 27 Myr and the period of core crystallisation is 4 Myr shorter  
 385 than for the constant case due to the increasing conductivity of the mantle.  
 386 The non-linear term in this case is negative, owing to the negative sign of  $\frac{dk}{dT}$ , and it am-  
 387 plifies the initial peak cooling rates at the depth examined (panel (d), Figure 5); how-  
 388 ever, the overall average cooling rate of the body is initially lower due to the low con-

**Table 3.** *Simple linear function for conductivity*

Model	Slope $\beta$ W/(m K <sup>2</sup> )	Reference $k_0$ W/(m K)	Average mantle $k$ W/(m K)	Core starts solidifying Myr	Duration of solidification Myr
Constant case	0.00	3.00	3.00	159.24 <sup>a</sup>	70.17 <sup>a</sup>
Positive $\beta$	0.0025	1.1125	3.02	140.52	72.79
Positive $\beta$ without non-linear term	0.0025	1.1125	2.77	113.62	55.40
Negative $\beta$	-0.0025	4.8875	3.16	186.37	66.11
Negative $\beta$ without non-linear term	-0.0025	4.8875	2.76	305.73	94.27

*Note:* Model results with a linear function for  $k$ . Regolith thickness is set to 0 km in all cases.

<sup>a</sup>As regolith is not included, note the earlier solidification than for the reference case with 8 km regolith, where the core starts solidifying at 171.58 Myr and the solidification period lasts 70.43 Myr.

ductivity (Figure 5f). When the non-linear term is neglected, the core begins to solidify 146 Myr later than in the constant case, and solidification takes 24 Myr longer. As the core does not freeze at the midpoint between the initial and surface temperatures, the non-linear terms for positive and negative  $\beta$  are not symmetric.

In summary, positive  $\beta$  leads to earlier onset of core freezing and a longer duration of core freezing, while negative  $\beta$  results in later onset of freezing and a shorter freezing period. For both  $\pm\beta$  the change in onset time when compared to the constant case is much larger than the change in the duration of core freezing, as there is a much greater difference between constant and variable  $k$  earlier in the model than during core solidification (Figures 5c, 5d). Even for linear conductivity functions with shallow slopes, the conductivity structure of the mantle is very different to that of the constant case and the temporal dependence of this structure has implications for the timing of events within the body that cannot be approximated by changing the value of  $k$  in the constant case. Inclusion of the non-linear term is essential as neglecting it can result in large over- or underestimations of core crystallisation onset time (for negative  $\beta$ , neglecting the non-linear term results in 119 Myr delay in the onset of core crystallisation). The implications of these results on the pallasite parent body are investigated using the experimentally derived functions in the next section.

### 3.3 Temperature-dependent properties: using experimental functions

The fully variable case, using the default parameters in Table 1 and the  $k(T)$ ,  $C(T)$  and  $\rho(T)$  functions (equations 9, 10 and 12), resulted in a 40 Myr delay in the onset of core crystallisation but only 3 Myr longer period of core crystallisation when compared to the reference case with constant properties (Figure 6). The temperature distribution in the shallow mantle is similar to that of the constant reference case, but the interior stays hotter for longer when  $T$ -dependent properties are used (Figure 6). The fully variable case requires deeper source regions for the pallasite meteorite samples than the reference case, with a depth of 61 km calculated for Imilac and 68 km for Esquel (Table 4).

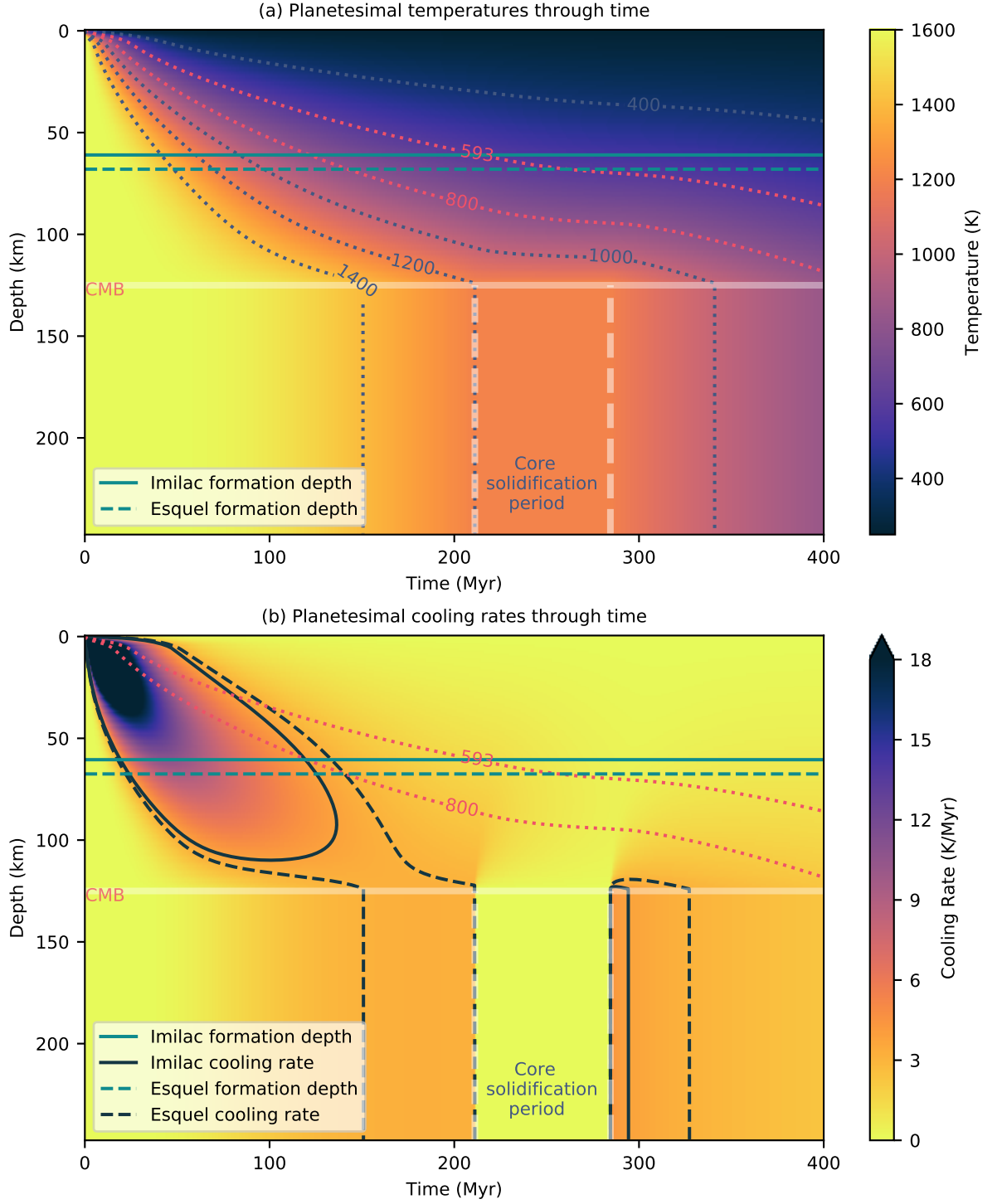


**Figure 6.** Planetesimal (a) temperatures and (b) cooling rates through time for a model with  $T$ -dependent  $k$ ,  $\rho$  and  $c$ . The calculated source depth of the Imilac and Esquel meteorites for this model set-up are shown in both plots, using the cooling rate data and method of Bryson et al. (2015). Temperature contours highlight the tetrataenite formation temperature when paleomagnetism can be recorded (593 K) and the temperature that corresponds to the sample’s measured cooling rates (800 K), while cooling rate contours show the measured cooling rates for both samples.

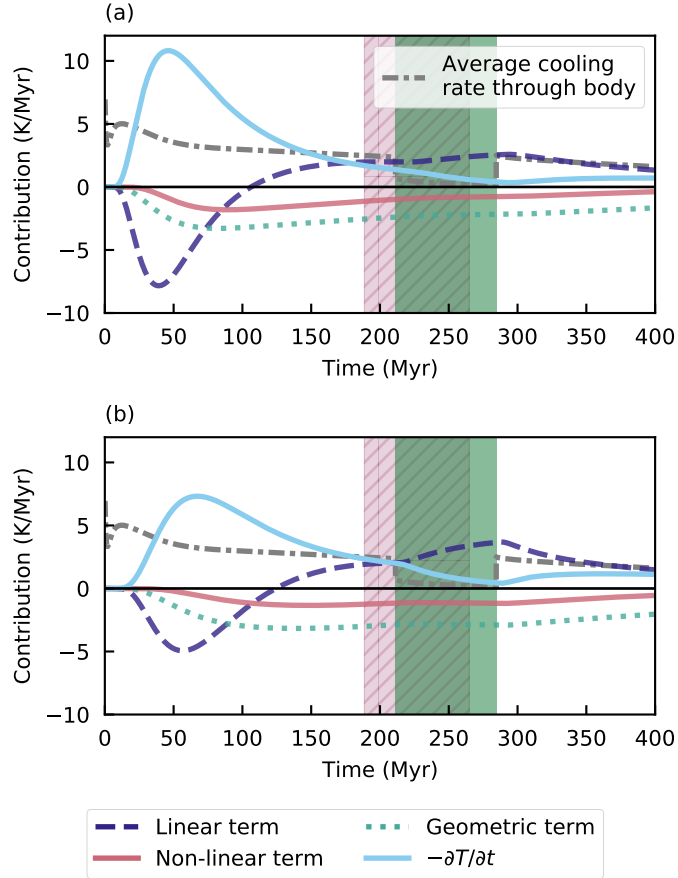


**Figure 7.** Results for the reference case with  $T$ -dependent  $k$ ,  $\rho$  and  $C$ . The components of the heat conduction equation are shown at a depth of (a) 42 km (one third of the thickness of the mantle) and (b) 84 km (two thirds). The cooling rate is multiplied by  $-1$  to illustrate how it balances the other components to add to zero. The green area defines the period of core crystallisation when  $T$ -dependent properties are used, while the pink area highlights the period of core crystallisation from the mean constant case for comparison.

417 When discussing simple linear functions for  $k(T)$ , we have demonstrated that cases  
 418 with constant and variable properties should be correctly calibrated in order to make mean-  
 419 ingful comparisons. In order to do so, we measured the average temperature in the mantle  
 420 of the fully variable case and used this to calculate new constant values of  $k$ ,  $C$  and  
 421  $\rho$  using equations 9, 10 and 12. The mean temperature of the mantle over the 400 Myr  
 422 of the model lifetime was 780 K, giving  $k = 2.8$  W/(m K),  $\rho = 2945$  kg/m<sup>3</sup> and  $C =$   
 423  $996$  J/(kg K). The model with constant properties was then rerun with these updated  
 424 values for  $k$ ,  $\rho$  and  $C$ , to more closely approximate the results from the fully variable model.  
 425 In this section, this new model using updated constant  $k$ ,  $\rho$  and  $C$  is referred to as the  
 426 constant mean values case, and the results are shown in table 4.

427 In the fully variable case (Figure 7), the non-linear term is negative and enhances  
 428 the overall cooling rate at the depths displayed for all times shown (up to 400 Myr), as  
 429 the slope of the function for  $k$  is negative for all  $T > 300$  K (Figure 1). A thin insu-  
 430 lating layer in the shallow mantle forms where  $T < 300$  K and the non-linear term is  
 431 positive. The core begins to freeze 211 Myr after model initiation, and takes 61 Myr to

**Table 4.** *Variable  $k$ ,  $\rho$  and  $c$ .*

Model	Core	Core	Imilac	Esquel	Imilac	Esquel
	Starts	Stops	depth	depth	timing	timing
	Myr	Myr	km	km	Myr	Myr
Reference (constant $k, \rho, c$ ) <sup>a</sup>	172	242	57	64	185	240
Constant (mean $k, \rho, c$ ) <sup>b</sup>	189	265	53	60	186	226
Variable <sup>c</sup>	211	285	61	68	206	248
Variable (non-linear = 0) <sup>d</sup>	245	335	47	54	190	234
Variable conductivity <sup>e</sup>	200	272	64	71	206	260
Variable heat capacity <sup>e</sup>	190	266	53	60	186	226
Variable density <sup>e</sup>	198	276	50	57	185	224

*Note:* Summary of key results. Timing of core crystallisation period given in millions of years after model start (myr) and formation depth of meteorites given in km. <sup>a</sup>Reference case with constant  $k = 3 \text{ W m}^{-1} \text{ K}^{-1}$ ,  $\rho = 3341 \text{ kg m}^{-3}$  and  $C = 819 \text{ J kg}^{-1} \text{ K}^{-1}$ . <sup>b</sup>Constant case here differs from the reference case: values for  $k$ ,  $\rho$  and  $c$  are calculated at the mean  $T$  in the fully variable case:  $k = 2.8 \text{ W m}^{-1} \text{ K}^{-1}$ ,  $\rho = 2945 \text{ kg m}^{-3}$ , and  $C = 996 \text{ J kg}^{-1} \text{ K}^{-1}$ . <sup>c</sup>Case with  $T$ -dependent  $k$ ,  $\rho$  and  $c$ . <sup>d</sup> $T$ -dependent properties, but with non-linear term neglected. <sup>e</sup>One property allowed to vary with  $T$  with other properties held at mean values as in <sup>b</sup>.

432 fully solidify. The constant mean values case does not replicate this result: with constant  
 433  $k$ ,  $\rho$  and  $C$ , the core begins to solidify at 189 Myr and takes 53 Myrs to fully freeze (Ta-  
 434 ble 4). In addition, the constant mean values case requires shallower source regions for  
 435 the pallasite meteorites Imilac and Esquel: 53 and 60 km respectively (Table 4). Qual-  
 436 itatively, the fully variable case is similar to the case with linear  $k$  and negative  $\beta$  in sec-  
 437 tion 3.2: the core begins to freeze later but takes a shorter time than the constant mean  
 438 values case (Tables 3 and 4). When the non-linear term is set to zero, again the fully vari-  
 439 able model behaves similarly to the  $\beta < 0$  linear case (Table 4).

440 When the different properties are allowed to vary in turn,  $T$ -dependent  $C$  produces  
 441 the smallest deviation in core crystallisation timing from the constant mean values case,  
 442 as at high  $T$  (temperatures such as those experienced by the planetesimals prior to and  
 443 during core crystallisation),  $C$  is approximately constant (Figure 1). Including variable  
 444  $\rho$  results in a 9 Myr delay in the onset and 2 Myr longer duration of core crystallisation  
 445 in comparison to the constant mean values case, while including only variable  $k$  results  
 446 in an 11 Myr delay in the onset and a 4 Myr shorter duration of core crystallisation. Vari-  
 447 able  $\rho$  produces the shallowest meteorite source regions of the three properties while vari-  
 448 able  $k$  produces the deepest (Table 4). Including just one  $T$ -dependent property cannot  
 449 replicate the fully variable model.

## 450 4 Discussion and Conclusion

451 Including  $T$ -dependent thermal properties changes the temperature structure in  
 452 the modelled planetesimal: predictions of mantle temperature can differ by 50 K over  
 453 tens of millions of years even when the best estimates for constant  $k$ ,  $\rho$  and  $C$  are used  
 454 (Figure 8). This results in significant changes in the timing and duration of core crys-  
 455 tallisation: the onset of core solidification is 22 Myr later, a delay of 12 %. We use the  
 456 example of a pallasite parent body to illustrate these results: including  $T$ -dependent prop-

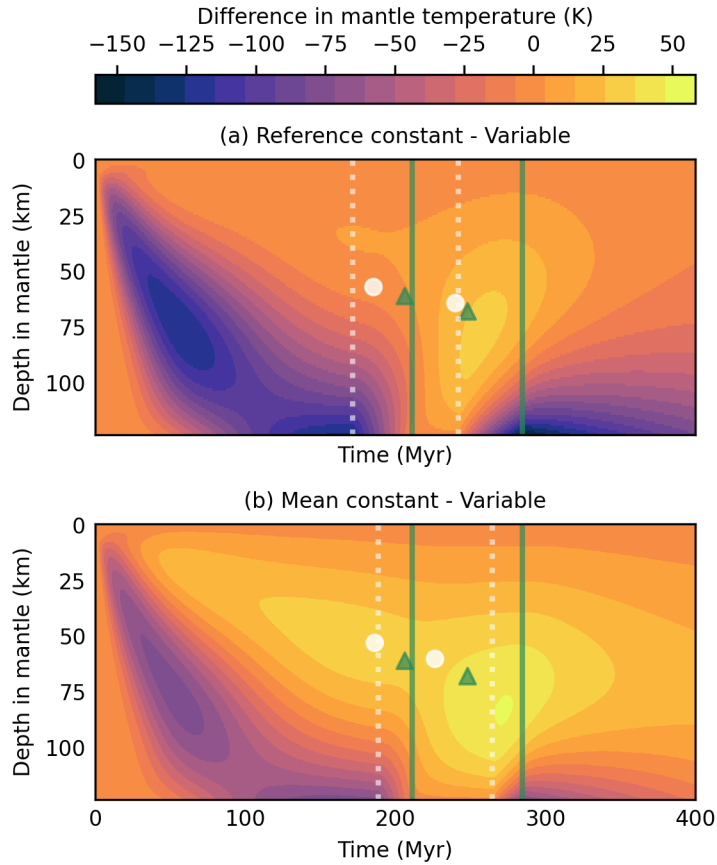


**Figure 8.** Difference in temperature distribution between (a) the reference constant model and variable model and (b) the mean constant model and variable model, where average  $k$ ,  $\rho$  and  $C$  through time and radius are equal. Period of core crystallisation is shown in dashed white for the constant cases, and in green for the variable case. Symbols mark the source regions for the Imilac and Esquel meteorites as they pass through the 593 K isotherm; white circles show the results from the constant cases, while green shows the result when variable properties are used. Cooling rate data from Bryson et al. (2015)

457 erties delays the onset of core crystallisation and results in deeper source regions for pal-  
 458 lasite meteorites than when constant  $k$ ,  $\rho$  and  $C$  are used (Figure 8). In this example,  
 459  $T$ -dependent  $k$ ,  $\rho$  and  $c$  result in a hotter deep mantle but cooler shallow mantle which  
 460 cannot be replicated by constant values (Figure 8).

461 Including  $T$ -dependent properties also affects whether or not samples are predicted  
 462 to preserve remnant magnetisation from a core dynamo: while in the constant reference  
 463 case both the Imilac and Esquel meteorite source depths cool through 593 K during core  
 464 freezing solidification, the Imilac region cools down below 593 K before core solidifica-  
 465 tion when variable  $k$ ,  $\rho$  and  $c$  or mean constant values based on the variable case are used  
 466 (Table 4). While the relative timing of the meteorite source regions' cooling through 593  
 467 K and the core crystallising can be reproduced by the constant mean case for this ex-  
 468 ample, the input values for  $k$ ,  $\rho$  and  $C$  require the fully variable case to be run initially  
 469 in order to be calculated.

470 In our example of a 250 km radius parent body, Imilac forms only  $\sim 5$  Myr before  
 471 the core begins to crystallise and so can be accounted for by error in the measurement  
 472 of the cooling rate from this sample (from Bryson et al. (2015)). However, larger discrep-  
 473 ancies in timing can be found for different cooling rates, parent body radii, regolith thick-  
 474 ness or core fraction (Figure 9). Including  $T$ -dependent properties narrows the range of  
 475 input parameters that allow meteorite samples to potentially record paleomagnetic sig-  
 476 natures. This provides a simple criteria for testing different parameter combinations: whether  
 477 the meteorite source region cools through the tetrataenite formation temperature dur-  
 478 ing core solidification. As shown in Figure 9, when constant  $k$ ,  $\rho$  and  $C$  are used, regolith  
 479 thicknesses anywhere between 0 – 12 km satisfy the above criteria for a planetesimal  
 480 of 250 km radius and a core that is 50% of  $r_p$ , while a regolith layer of 4 - 8 km is re-  
 481 quired when  $T$ -dependent properties are used. If the core fraction is reduced to 30% of  
 482  $r_p$ , a 250 km body with regolith between 0 - 8 km can accommodate both meteorite sam-  
 483 ples, whereas no suitable combination of parameters can be chosen when  $T$ -dependent  
 484  $k$ ,  $\rho$  and  $c$  are used. Similarly, no suitable parent body with a 250 km radius and a core  
 485 fraction of 70%  $r_p$  can be found if  $T$ -dependent properties are used, whereas if these val-  
 486 ues are taken as constant, then a planetesimal with a radius of 300 km including an 8  
 487 km thick regolith can produce the cooling rates and required timings in both meteorites.

488 One limitation of this work is the simplified core crystallisation model used.  $T$ -dependent  
 489 properties have not been addressed for this region. Future work could develop or incor-  
 490 porate a more sophisticated core cooling and crystallisation model, to address issues such  
 491 as directionality of crystallisation which may have implications for the interpretation of  
 492 paleomagnetic signatures recorded in meteorite suites. Following crystallisation, the core  
 493 is assumed to return to an isothermal state due to the high conductivity of the mate-  
 494 rial. For the pallasite example case, this is an acceptable simplification as it is the times  
 495 preceding and during the core solidification period that are of interest. For other appli-  
 496 cations it may be required to restart the model with the core included in the iterative  
 497 solution with a Neumann boundary condition at the centre, as used for approximating  
 498 the analytical solution (see Supplementary Information). The effects of pressure and grav-  
 499 ity have also been neglected due to the low pressure gradient expected within the body  
 500 as discussed in section 1.

501 In conclusion,  $T$ -dependent properties can significantly impact the output of plan-  
 502 etesimal cooling models, even if the model results are being used qualitatively or to judge  
 503 the relative timing of processes within the body, such as whether meteorite formation  
 504 regions cool through specific temperatures before, during or after the period of core crys-  
 505 tallisation. The inclusion of  $T$ -dependent  $k$ ,  $\rho$  and  $C$  results in later crystallisation of the  
 506 core ( $\sim 40$  Myr later than the constant reference case and  $\sim 20$  Myr later than the up-  
 507 dated constant case) and deeper meteorite formation depths due to suppressed cooling  
 508 rates in the mantle. This result cannot be replicated with constant values for  $k$ ,  $\rho$  and  
 509  $C$ , even when these values are chose to match the mean values of each through time and

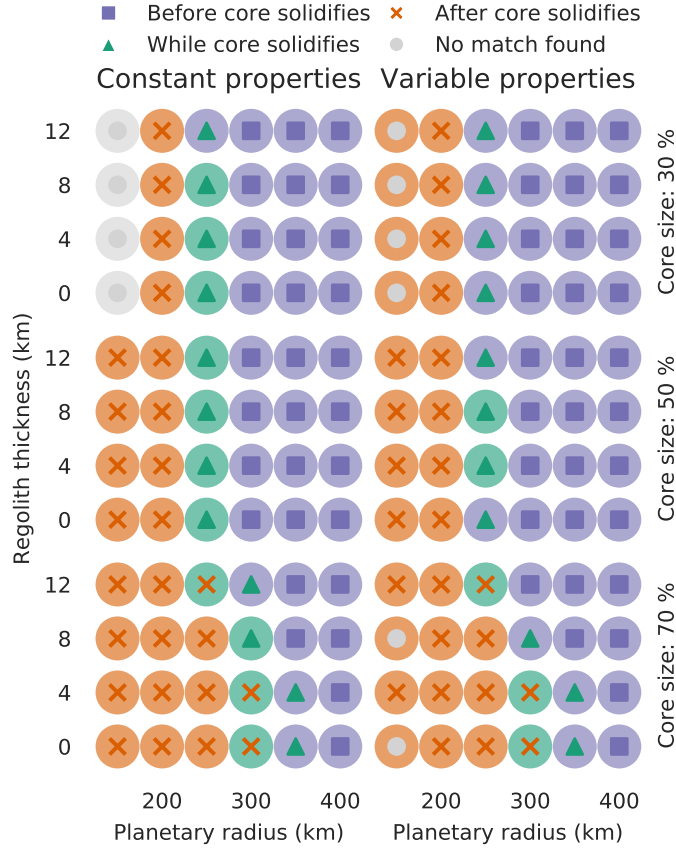


**Figure 9.** Planetary radius, core size and regolith thickness investigation for the constant  $k$ ,  $\rho$  and  $C$  case, and the fully variable case. The small symbols represent the Esquel meteorite, while the larger circles represent Imilac. The colour and symbol denote whether or not the meteorite source region cooled through 593 K during core crystallisation  $\pm 10$  Myr: green circles or triangles mark models where this criteria was met. Red circles or crosses denote models where the meteorite cooled through 593 K after core crystallisation, whereas blue circles or squares show where this happened before the core began to crystallise. Grey markers note that no matches for the meteorite cooling rates at 800 K were found, implying the meteorite could not have formed in that body. Cooling rate data from Bryson et al. (2015).

510 radius in the variable model. If  $T$ -dependent  $\kappa$  is included without a non-linear term,  
 511 the reduction in cooling rates through the body is overestimated, resulting in core so-  
 512 lidification 33 Myr after the variable case and 73 Myr after the constant case. These re-  
 513 sults are shown with relevance to the pallasite parent body. The parameter space which  
 514 satisfies the cooling rate criteria for the material which formed the Imilac and Esquel me-  
 515 teorites shrinks when  $T$ -dependent properties are included; it follows that if more sam-  
 516 ples are investigated the parameter space will shrink further. Future work could use this  
 517 more restrictive parameter space to address the ongoing debate over the number of re-  
 518 quired pallasite parent bodies and potentially place a minimum constraint on the num-  
 519 ber of bodies required.  $T$ -dependent properties should also be addressed for other plan-  
 520 etesimals and meteorite parent bodies where conduction is involved, for example the or-  
 521 dinary chondrite parent body, where peak temperatures and the inferred parent body  
 522 radius may be incorrectly calculated.

### 523 Acknowledgments

524 Data availability: representative model output data are publically available from the Na-  
 525 tional Geoscience Data Centre (NGDC), the Natural Environment Research Council (UK)  
 526 data centre for geoscience data, under the ID 138605. Model is described in detail in the  
 527 main text with all parameters used to allow for reproduction. MMQ was supported by  
 528 the Leeds-York Natural Environment Research Council Doctoral Training Partnership  
 529 (NE/L002574/1). CJD was supported by Natural Environment Research Council Inde-  
 530 pendent Research Fellowship (NE/L011328/1).

### 531 References

- 532 Akridge, G., Benoit, P. H., & Sears, D. W. (1998). Regolith and megaregolith  
 533 formation of h-chondrites: Thermal constraints on the parent body. *Icarus*,  
 534 *132*(1), 185–195.
- 535 Allan, D., & Jacobs, J. (1956). The melting of asteroids and the origin of meteorites.  
 536 *Geochimica et Cosmochimica Acta*, *9*(5-6), 256–272.
- 537 Baker, J., Bizzarro, M., Wittig, N., Connelly, J., & Haack, H. (2005). Early plan-  
 538 etesimal melting from an age of 4.5662 Gyr for differentiated meteorites. *Na-  
 539 ture*, *436*(7054), 1127–1131.
- 540 Bennett, M. E., & McSween, H. Y. (1996). Revised model calculations for the ther-  
 541 mal histories of ordinary chondrite parent bodies. *Meteoritics & Planetary Sci-  
 542 ence*, *31*(6), 783–792.
- 543 Berman, R. G., & Brown, T. H. (1985). Heat capacity of minerals in the system  
 544  $\text{Na}_2\text{O}-\text{K}_2\text{O}-\text{CaO}-\text{MgO}-\text{FeO}-\text{Fe}_2\text{O}_3-\text{Al}_2\text{O}_3-\text{SiO}_2-\text{TiO}_2-\text{H}_2\text{O}-\text{CO}_2$ : repre-  
 545 sentation, estimation, and high temperature extrapolation. *Contributions to  
 546 Mineralogy and Petrology*, *89*(2), 168–183.
- 547 Boss, A. P. (1998). Temperatures in protoplanetary disks. *Annual Review of Earth  
 548 and Planetary Sciences*, *26*(1), 53–80.
- 549 Bryson, J. F. J., Nichols, C. I. O., Herrero-Albillos, J., Kronast, F., Kasama,  
 550 T., Alimadadi, H., ... Harrison, R. J. (2015). Long-lived magnetism  
 551 from solidification-driven convection on the pallasite parent body. *Nature*,  
 552 *517*(7535), 472–475.
- 553 Carslaw, H. S., & Jaeger, J. C. (1986). *Conduction of heat in solids* (2nd ed ed.).  
 554 Oxford : New York: Clarendon Press ; Oxford University Press.
- 555 Crank, J. (1979). *The mathematics of diffusion*. Clarendon Press.
- 556 Davies, C. J., & Pommier, A. (2018). Iron snow in the martian core? *Earth and  
 557 Planetary Science Letters*, *481*, 189–200.
- 558 Debye, P. (1912). Zur Theorie der spezifischen Wärmen. *Annalen der Physik*,  
 559 *344*(14), 789–839.
- 560 Elkins-Tanton, L. T., Weiss, B. P., & Zuber, M. T. (2011). Chondrites as samples of

- 561 differentiated planetesimals. *Earth and Planetary Science Letters*, 305(1-2), 1–  
562 10.
- 563 Fei, Y. (2013). Thermal expansion. In *Mineral physics & crystallography* (p. 29-44).  
564 American Geophysical Union (AGU).
- 565 Fu, R. R., Hager, B. H., Ermakov, A. I., & Zuber, M. T. (2014). Efficient early  
566 global relaxation of asteroid vesta. *Icarus*, 240, 133–145.
- 567 Gail, H.-P., Tieloff, M., Breuer, D., & Spohn, T. (2014). Early thermal evolution of  
568 planetesimals and its impact on processing and dating of meteoritic material.  
569 In *Protostars and planets VI*. University of Arizona Press.
- 570 Ghosh, A., & McSween, H. Y. (1998). A thermal model for the differentiation of as-  
571 teroid 4 vesta, based on radiogenic heating. *Icarus*, 134(2), 187–206.
- 572 Ghosh, A., & McSween, H. Y. (1999). Temperature dependence of specific heat ca-  
573 pacity and its effect on asteroid thermal models. *Meteoritics & Planetary Sci-  
574 ence*, 34(1), 121–127.
- 575 Greenwood, R. C., Burbine, T. H., & Franchi, I. A. (2020). Linking asteroids and  
576 meteorites to the primordial planetesimal population. *Geochimica et Cos-  
577 mochimica Acta*, 277, 377–406.
- 578 Haack, H., Rasmussen, K. L., & Warren, P. H. (1990). Effects of re-  
579 golith/megaregolith insulation on the cooling histories of differentiated as-  
580 teroids. *Journal of Geophysical Research*, 95(B4), 5111–5124.
- 581 Harrison, K. P., & Grimm, R. E. (2010). Thermal constraints on the early history of  
582 the h-chondrite parent body reconsidered. *Geochimica et Cosmochimica Acta*,  
583 74(18), 5410–5423.
- 584 Hevey, P. J., & Sanders, I. S. (2006). A model for planetesimal meltdown by 26-al  
585 and its implications for meteorite parent bodies. *Meteoritics & Planetary Sci-  
586 ence*, 41(1), 95–106.
- 587 Hofmeister, A. M. (1999). Mantle values of thermal conductivity and the geotherm  
588 from phonon lifetimes. *Science*, 283(5408), 1699–1706.
- 589 Hort, M. (1997). Cooling and crystallization in sheet-like magma bodies revisited.  
590 *Journal of Volcanology and Geothermal Research*, 76(3-4), 297–317.
- 591 Isaak, D. G. (1992). High-temperature elasticity of iron-bearing olivines. *Journal of  
592 Geophysical Research: Solid Earth*, 97(B2), 1871–1885.
- 593 Johnson, B. C., Sori, M. M., & Evans, A. J. (2019). Ferrovolcanism on metal worlds  
594 and the origin of pallasites. *Nature Astronomy*, 4(1), 41–44.
- 595 Kokubo, E., & Ida, S. (2012). Dynamics and accretion of planetesimals. *Progress of  
596 Theoretical and Experimental Physics*, 2012(1).
- 597 MacPherson, G. J. (2014). Calcium–Aluminum-Rich Inclusions in Chondritic Me-  
598 teorites. In A. M. Davis (Ed.), *Volume 1 of treatise on geochemistry (second  
599 edition): Meteorites and cosmochemical processes* (p. 139–179). Elsevier-  
600 Pergamon.
- 601 Miyamoto, M., Fujii, N., & Takeda, H. (1982). Ordinary chondrite parent body - An  
602 internal heating model. *Lunar and Planetary Science Conference Proceedings*,  
603 12, 1145-1152.
- 604 Moskovitz, N., & Gaidos, E. (2011). Differentiation of planetesimals and the thermal  
605 consequences of melt migration. *Meteoritics & Planetary Science*, 46(6), 903–  
606 918.
- 607 Özisik, M. (1993). *Heat conduction*. New York: Wiley.
- 608 Petit, A.-T., & Dulong, P.-L. (1819). Recherches sur quelques points importants de  
609 la théorie de la chaleur. *Annales de Chimie et de Physique*, 10, 395–413.
- 610 Poirier, J.-P. (2000). *Introduction to the Physics of the Earth's Interior*. Cambridge:  
611 Cambridge University Press.
- 612 Robie, R. A., Hemingway, B. S., & Takei, H. (1982). Heat capacities and entropies  
613 of Mg<sub>2</sub>SiO<sub>4</sub>, Mn<sub>2</sub>SiO<sub>4</sub>, and Co<sub>2</sub>SiO<sub>4</sub> between 5 and 380 K. *American Mineral-  
614 ogist*, 67(5-6), 470–482.
- 615 Sahijpal, S., Soni, P., & Gupta, G. (2007). Numerical simulations of the differentia-

- tion of accreting planetesimals with  $^{26}\text{Al}$  and  $^{60}\text{Fe}$  as the heat sources. *Meteoritics & Planetary Science*, 42(9), 1529–1548.
- Scheinberg, A., Soderlund, K., & Schubert, G. (2015). Magnetic field generation in the lunar core: The role of inner core growth. *Icarus*, 254, 62–71.
- Seipold, U. (1998). Temperature dependence of thermal transport properties of crystalline rocks — a general law. *Tectonophysics*, 291(1-4), 161–171.
- Solomon, S. C. (1979). Formation, history and energetics of cores in the terrestrial planets. *Physics of the Earth and Planetary Interiors*, 19(2), 168–182.
- Su, C., Liu, Y., Song, W., Fan, D., Wang, Z., & Tang, H. (2018). Thermodynamic properties of San Carlos olivine at high temperature and high pressure. *Acta Geochimica*, 37(2), 171–179.
- Suzuki, I. (1975). Thermal Expansion of Periclase and Olivine, and their Anharmonic Properties. *Journal of Physics of the Earth*, 23(2), 145–159.
- Tarduno, J. A., Cottrell, R. D., Nimmo, F., Hopkins, J., Voronov, J., Erickson, A., ... McKinley, R. (2012). Evidence for a Dynamo in the Main Group Pallasite Parent Body. *Science*, 939(315), 1427–1798.
- The OSIRIS-REx Team, DellaGiustina, D. N., Emery, J. P., Golish, D. R., Rozitis, B., Bennett, C. A., ... Lauretta, D. S. (2019). Properties of rubble-pile asteroid (101955) Bennu from OSIRIS-REx imaging and thermal analysis. *Nature Astronomy*, 3(4), 341–351.
- Warren, P. H. (2011). Ejecta-megaregolith accumulation on planetesimals and large asteroids. *Meteoritics & Planetary Science*, no–no.
- Wen, H., hui Lu, J., Xiao, Y., & Deng, J. (2015). Temperature dependence of thermal conductivity, diffusion and specific heat capacity for coal and rocks from coalfield. *Thermochimica Acta*, 619, 41–47.
- Williams, J.-P., & Nimmo, F. (2004). Thermal evolution of the martian core: Implications for an early dynamo. *Geology*, 32(2), 97.
- Woolum, D. S., & Cassen, P. (1999). Astronomical constraints on nebular temperatures: Implications for planetesimal formation. *Meteoritics & Planetary Science*, 34(6), 897–907.
- Xu, Y., Shankland, T. J., Linhardt, S., Rubie, D. C., Langenhorst, F., & Klasinski, K. (2004). Thermal diffusivity and conductivity of olivine, wadsleyite and ringwoodite to 20 GPa and 1373 K. *Physics of the Earth and Planetary Interiors*, 143-144, 321–336.
- Yang, C. W., Williams, D. B., & Goldstein, J. I. (1997). A new empirical cooling rate indicator for meteorites based on the size of the cloudy zone of the metallic phases. *Meteoritics & Planetary Science*, 32(3), 423–429.
- Yang, J., Goldstein, J. I., & Scott, E. R. (2010). Main-group pallasites: Thermal history, relationship to IIIAB irons, and origin. *Geochimica et Cosmochimica Acta*, 74(15), 4471–4492.
- Yomogida, K., & Matsui, T. (1983). Physical properties of ordinary chondrites. *Journal of Geophysical Research: Solid Earth*, 88(B11), 9513–9533.
- Young, H. D. (1991). *University physics* (8th ed.). New York: Addison-Wesley.
- Zhang, Y., Yoshino, T., Yoneda, A., & Osako, M. (2019). Effect of iron content on thermal conductivity of olivine with implications for cooling history of rocky planets. *Earth and Planetary Science Letters*, 519, 109–119.